



Damage mapping with a degrading elastic modulus using piezospectroscopic coatings



Gregory Freihofe^{a,*}, Axel Schülzgen^b, Seetha Raghavan^a

^a Mechanical and Aerospace Engineering Department, University of Central Florida, 4000 Central Florida Blvd., Orlando, FL 32816, USA

^b CREOL, The College of Optics and Photonics, University of Central Florida, 4000 Central Florida Blvd., Orlando, FL 32816, USA

ARTICLE INFO

Article history:

Received 24 March 2015

Received in revised form

12 July 2015

Accepted 13 July 2015

Available online 26 July 2015

Keywords:

Piezospectroscopy

Mechanical properties

Multiscale mechanics

Damage mechanics

Non-destructive evaluation

ABSTRACT

The development of piezospectroscopic (PS) composites has enabled the creation of a non-destructive evaluation (NDE) technique which integrates piezospectroscopy, digital image correlation (DIC) and analytical multi-scale mechanics to map the elastic modulus of a coated material. The measured elastic modulus was represented as a normal distribution with a mean value (32.2 GPa) which is within 8% of the conventionally recorded modulus (35 GPa). Damage mechanics are applied to map elastic degradation *in situ* mechanical loading with an average uncertainty (~ 10 GPa) that was sufficient in observing subsurface, progressive damage patterns which are unique to the coated material.

© 2015 Elsevier Ltd. All rights reserved.

1. Introduction

Detecting damage with NDE is an important field for the diagnosis of structural health with applications ranging from aerospace [1] to civil [2] structures. Conventional NDE techniques are based on the identification of the size and location of defects. Techniques such as ultrasound [3], thermography [4], shearography [5], and others [6] are technologies that each have their own set of advantages in this regard.

An alternative way of monitoring damage is by quantifying the reduced mechanical properties. The presence of micro-voids or cracks creates a softening effect which decreases the elastic modulus of the continuum [7]. When compared to a variety of damage measures, monitoring the degrading elastic modulus is a promising technique [8]. The degraded elastic modulus can be captured experimentally with the slope of an unloading curve or predicted with a damage model. The major weakness is that it lacks the capacity to detect local damage because a measure of the elastic modulus is conventionally a nominal or macroscopic measure.

In laboratory settings, determining nominal mechanical properties is straightforward with a load cell, strain gage, and standard test specimens. However, evaluating local mechanical properties of a structure would require a combination of stress and strain mapping. Strain mapping is available with a few techniques including electronic speckle pattern interferometry [9], Moiré interferometry [10], and

digital image correlation (DIC) [11]. Stress mapping with the same flexibilities as the previously mentioned strain mapping techniques has not been available, until now, with piezospectroscopy. This work shows that piezospectroscopy, recorded over a field of view, can couple with strain maps to locally distinguish elastic moduli, thereby removing the weakness this damage measure is nominal.

Other approaches to estimate local mechanical properties are available such as atomic force microscopy [12,13] and ultrasonic [14] methods. These techniques rely on other physical principles to determine the elastic modulus rather than conventional stress/strain relationships and are currently active fields of research [15,3]. Among these, however, piezospectroscopy stands out as the one technique suitable enough for integration with full-scale mechanical load frames for standard coupon testing [16,17].

Piezospectroscopy with Cr doped Al_2O_3 has been most widely used as a pressure sensor in diamond anvil cells [18], and as an NDE technique for monitoring the health of thermal barrier coatings [19]. The applications of piezospectroscopy have recently been expanded by the fabrication of alumina-epoxy nanocomposites with tailorable mechanical and PS properties [20]. This produced a material which can be applied as a compliant coating to structures for stress sensing [21–23]. In the process of holistically understanding the multi-scale mechanics of these new materials, the solution of an effective elastic modulus of the nanocomposite with the experimental PS response was discovered [24]. In this work, multi-scale mechanics are extended to a nanocomposite coating, to solve for an effective elastic modulus of the composite substrate *in situ* mechanical loading.

* Corresponding author.

E-mail address: Freihofe@knights.ucf.edu (G. Freihofe).

2. Experiment

The PS nanocomposite coating investigated in this work was manufactured by Elantas PDG, Inc. by mixing 150 nm, Cr doped α - Al_2O_3 nanoparticles (Inframat Corp.) with 99.8% purity in epoxy to achieve a 20% volume fraction of particles. The coating was applied to a composite substrate consisting of laminated IM7-8552 unidirectional tape (57.7% fiber volume) manufactured with a $[45/-45/0/45/-45/90/45/-45/45/-45]_s$ layup resulting in transversely isotropic properties ($E_1 = E_2 = 35$ GPa) [25]. The coating has a very small thickness (300 μm) and low modulus (< 1 GPa) which ensures that it does not mechanically reinforce the composite substrate. The coated sample was machined and tested in accordance with composite open hole tension (OHT) ASTM standards [26]. The length, width, thickness and hole size of the coupon were 12, 1.5, 0.15, and 0.25 in respectively.

The sample was loaded at a rate of 0.05 in/min (0.127 cm/min) and held using displacement control using a hydraulic load frame at 10 load points throughout the experiment as marked in Fig. 1. This avoided creep during the higher loads, but prompted stress relaxation which was acceptable since the goal was to observe damage progression. During each hold, PS and DIC measurements were collected on the front and the back side of the substrate, respectively. Both measurements can be directly compared since the substrate has a symmetric layup, shown in Fig. 1.

PS data was collected with a prototype portable spectrometer system designed to be easily transported with a quick setup time [17]. Excitation was achieved using a low power, 1.5 mW laser of 532 nm wavelength in a back scattering configuration with a long working distance objective (28 mm). The photoluminescence (PL) spectra were collected on a 60×60 grid during a snake scan, implemented using a synchronized translation stage, with the accumulation time for spectra at 100 ms. The total measurement area was 25.4 mm squared, corresponding to a spatial resolution of 0.4 mm in both directions of the measurement plane. With these settings each map is collected within 8 min.

The DIC measurements were collected at the beginning of every hold and were relatively instantaneous. The speckle pattern, which was spray painted, had an average dot size of roughly

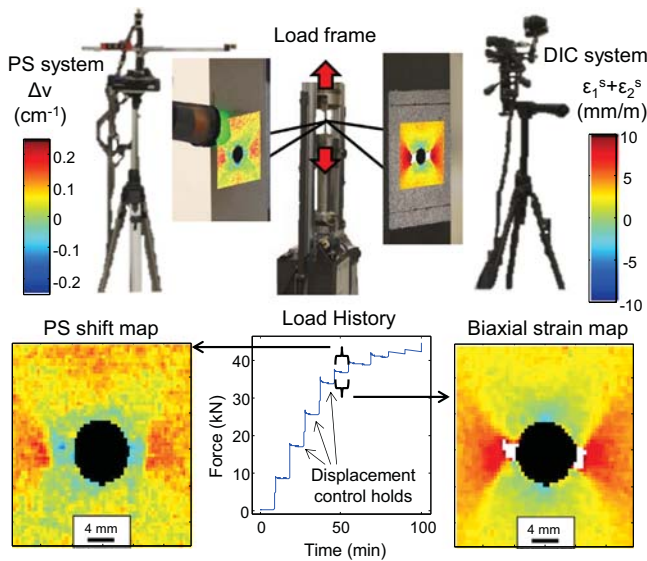


Fig. 1. Both PS and DIC tripod systems are measuring the stress and strain field respectively on opposing sides of the composite coupon in a mechanical load frame. The steps within the load history graph are displacement control holds, which were necessary to prevent creep in the sample at the high failure loads during mapping the PS response. This resulted in a softening of the material during and is observed as a reduction in force during the load steps.

0.2 mm. The DIC images were post processed to have a spatial resolution equal to that of the PS maps (0.4 mm). Furthermore, a post-processing algorithm was created to spatially match up the DIC and PS mapping data. In brevity, the algorithm interpolated data on a new coordinate system using the open hole as a reference. The accuracy of the pixel match up is worst in regions closest to the open hole (≤ 0.4 mm) but is negligible at a few pixels distance away (1–2) [27].

3. Multiscale mechanics to model the PS response

Spatial measurements of substrate strain and PS shift were obtained simultaneously for the first time in a novel experiment [23]. The PS relationships originate from the distortion of the Ligand field around the Cr^{3+} substitutional impurity within the Al_2O_3 lattice. As the lattice is deformed under mechanical load, the energy levels of the Ligand field change, resulting in a frequency shift of the photo-stimulated luminescence [28]. Usually, the PS relationships are dependent on crystallographic orientation, but for a polycrystalline material whose grain size is an order of magnitude smaller than the probed volume (i.e. laser dot size) an averaging effect takes place and simplifies the PS relationship to be a function of the first stress or strain invariant [29]. In this study, the PS shift is considered as the mean shift of the R1 and R2 spectral lines, which has been associated to the first stress invariant [24,30].

Here, the PS response is taken as the substrate's DIC biaxial strain ($\epsilon_1^s + \epsilon_2^s$) vs. PS shift ($\Delta\nu$). When evaluating this relationship, a variety of mechanics have to be considered as illustrated in Fig. 2. For linear elastic behavior, a PS response is described by the composite's PS coefficient (Π_c) in $\Delta\nu = \Pi_c(\epsilon_1^s + \epsilon_2^s)$

This PS coefficient is experimentally measured for every pixel when the PS shift and DIC biaxial strain maps are combined. This experimental PS coefficient represents a combination of several mechanics that describe the process when load is transferred from the substrate to the coating to the particle. The series of ratios that describe this PS coefficient are shown in the following equation:

$$\Pi_c = \frac{\Delta\nu \epsilon_{ii}^p}{\epsilon_{ii}^p \epsilon_{ii}^c \epsilon_1^s + \epsilon_2^s} \quad (1)$$

The first ratio encompasses the relationship between the mean R-line shift with the particle's first strain invariant (ϵ_{ii}^p) as shown in Eq. (2). This is a variation of the equation that commonly uses the first stress invariant (σ_{ii}) with the PS shift by the trace of PS tensor ($\Pi_{ii} = 7.6 \text{ cm}^{-1}/\text{GPa}$) [31]. The first stress and strain invariant is interchangeable with the bulk modulus of the particle (K^p) using the relation $3K\epsilon_{ii} = \sigma_{ii}$

$$\frac{\Delta\nu}{\epsilon_{ii}^p} = \Pi_{ii} K^p \quad (2)$$

The second ratio describes the relationship between the first strain invariant of the particle and coating. This equation was derived using Eshelby's inclusion mechanics [24] which assumed a spherical particle, and both phases are isotropic. The ratio is a function of the properties for the coating (E^c, ν^c) and particle (E^p, ν^p) shown in the following equation:

$$\frac{\epsilon_{ii}^p}{\epsilon_{ii}^c} = \frac{-3E^c(2\nu^p - 1)(\nu^c - 1)}{(2\nu^c - 1)(2E^c + E^p - 4E^c\nu^p + E^p\nu^c)} \quad (3)$$

The last ratio describes the relationship between the first invariant of the coating with the biaxial strain of the substrate. A number of steps are associated with obtaining this ratio which are outlined elsewhere [27] and are valid for a thin compliant coating. Briefly, the expression is obtained by equating interface strains ($\epsilon_1^s = \epsilon_1^c, \epsilon_2^s = \epsilon_2^c$) between the isotropic coating and transversely isotropic substrate under plane stress ($\sigma_3 = \sigma_3^c = 0$). In addition,

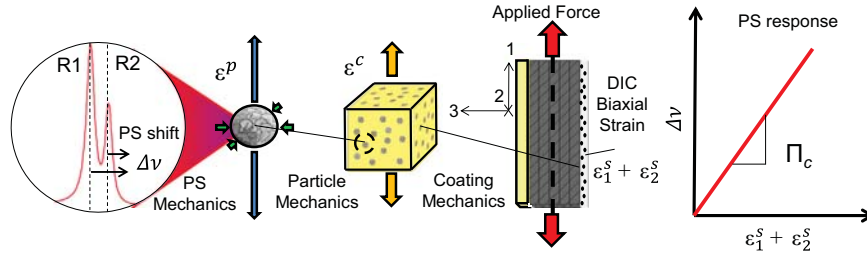


Fig. 2. A summary of the multiscale mechanics to describe the nanocomposite coating problem.

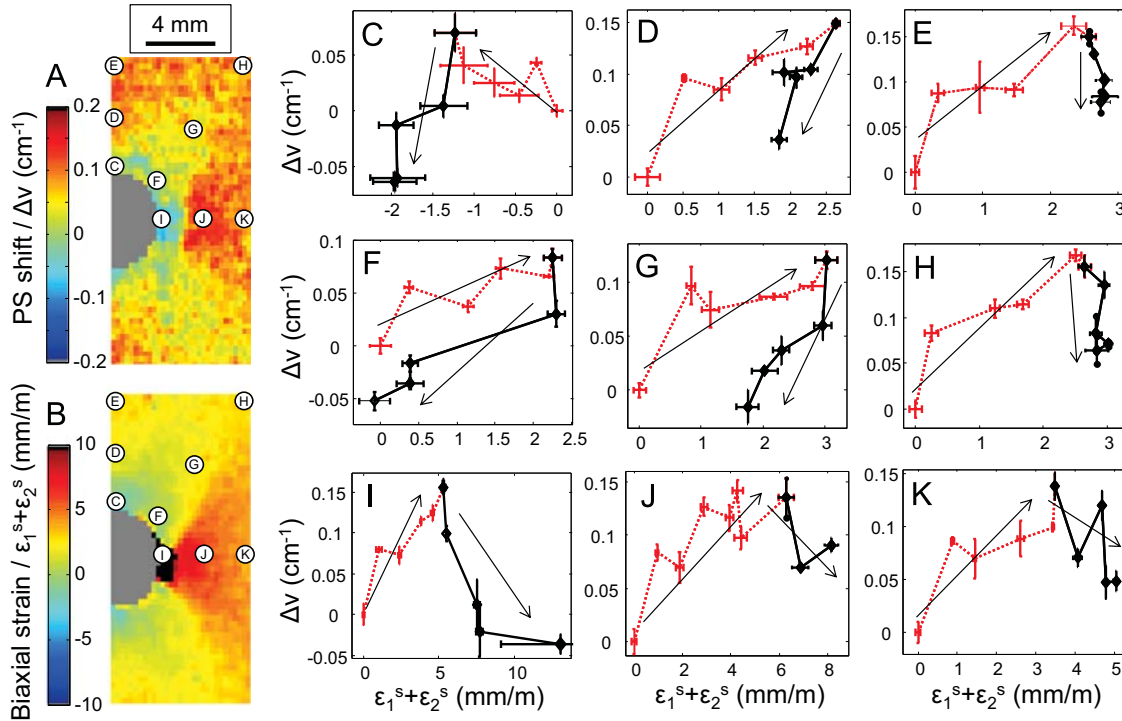


Fig. 3. (A) PS shift and (B) biaxial strain maps for half of the open hole. (C–L) A variety of local PS responses, each representing a 400 μm square area from indicated locations labeled on the PS and DIC maps. The x and y error bars represent spatial variations during an alignment and interpolation algorithm which combined the PS and DIC data sets discussed in the experiment section.

the expression $e_{ii}^s / (e_1^s + e_2^s) = (1 - 2\nu^s) / (1 - \nu^s)$ is used which is valid for a transversely isotropic material in plane stress. The result is only a function of Poisson's ratio for the coating (ν^c) and substrate (ν^s), given in the following equation:

$$\frac{e_{ii}^c}{e_1^s + e_2^s} = \frac{(1 - \nu^s - \nu^{s2})(1 - \nu^s)(1 + \nu^s)(1 - 2\nu^s)}{(1 - \nu^c - \nu^{c2})(1 - \nu^c)^2(1 + \nu^c)} \quad (4)$$

The series of ratios that describe the PS coefficient have now been described and is a function as follows: $\Pi_c = f(\Pi_{ii}, E^p, \nu^p, E^c, \nu^c, \nu^s)$. After all of the applied mechanics, the PS coefficient was not a function of the elastic modulus of the substrate (E^s). To obtain an expression which includes E^s , and solely a function thereof requires a set of assumptions:

1. The strain which the substrate experiences is directly transferred into the particles. This is appropriate with a compliant coating with low elastic modulus and thickness, providing no mechanical reinforcement. This enables the removal of the coating mechanics term and the replacement of the coating's isotropic properties with the substrate's in Eq. (3). Therefore

$$\Pi_c = f(\Pi_{ii}, E^p, \nu^p, E^s, \nu^s)$$

2. The particle's properties are known ($E^p = 400 \text{ GPa}$, $\nu^p = 0.23$). A variation of particle properties among literature [32–35] has resulted in a conservative uncertainty reported in the Appendix. Π_{ii} is also considered a property of the particle. Therefore

$$\Pi_c = f(E^s, \nu^s)$$

3. Isotropic damage assumes that Poisson's ratio does not change [36], and the substrate's pristine Poisson's ratio can be estimated using classical laminate plate theory [37] ($\nu^s = 0.57$). Therefore

$$\Pi_c = f(E^s)$$

The first assumption makes the substrate isotropic. The challenge is to modify the Eshelby tensor for a transversely isotropic media [38]. For this application, it is desired to solve the Eshelby tensor symbolically, in order to rearrange Eshelby's equation for the matrix's elastic modulus, as was done recently for an isotropic media [24]. The complexity of the explicit solution for a transversely isotropic Eshelby tensor, and lack thereof for a generic anisotropic case [39], results in a challenging undertaking to remove the isotropic substrate assumption.

With the above assumptions, a refined series of ratios can now be combined and rearranged to solve for the substrate's elastic modulus. This leaves a direct solution of the substrate's elastic modulus with an experimental measure of the first order PS coefficient (Π_c) from the PS response

$$E^s = \frac{E^p \Pi_c (\nu^s + 1)}{2\Pi_c - 3K^p \Pi_{ii} (2\nu^p - 1)} \quad (5)$$

The character of the PS responses vary depending on their location with respect to the open hole. In Fig. 3, the variation in the PS responses is attributed to the non-proportional and non-uniform loading across the sample's surface. This, combined with the relatively few data points at low loads, makes for a challenge in determining the first order approximation of Π_c .

The composite substrate will have linear elastic behavior until fracture. This is dissimilar to the high volume fraction nanocomposite coating (20%) which has inelastic properties [40,32]. This explains the non-linearity in the PS response, but makes it difficult to quantify Π_c for the elastic modulus calculation.

To have a robust method of obtaining Π_c for every PS response, a yield function is fit to a segment of the PS response from zero load until the maximum PS shift. A Ramberg–Osgood yield function was used because it works well without a well defined yield point [41]. This yield function is normally used for a strain–stress plot, but was modified here for a strain–PS shift plot in Eq. (6). This reformulation of the Ramberg–Osgood formula is appropriate because the PS shift is directly proportional to the strain as derived in the previous section. For brevity, $e_b = \epsilon_1 + \epsilon_2$

$$\Delta\nu = \Pi_c e_b + \alpha e_{by} \Pi_c \left(\frac{e_b}{e_{by}} \right)^m \quad (6)$$

Eq. (6) was fitted to every local PS response such as shown in Fig. 4. The Π_c value as solved by the fitting algorithm varied significantly across the surface due to the sparse number of data points at low loads and was not suitable to solve for E^s . Due to the need to have a more consistent estimation of Π_c , the yield function was used to interpolate a derivative of the PS response at a very small strain for all of the PS responses. This would be the approximation of the first order PS coefficient before the non-linearity initiated. The strain chosen to evaluate the derivative of the yield function and compute Π_c was chosen to be 0.025 mm/m for all PS responses and is marked in Fig. 4.

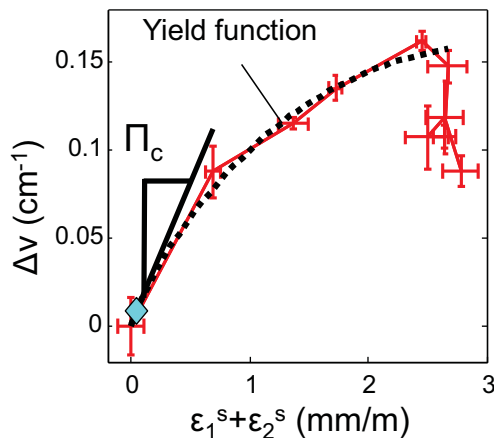


Fig. 4. The yield function is marked on the PS response with a marker designating the strain at 0.025 mm/m which the derivative was evaluated to calculate Π_c .

4. Elastic modulus and damage mapping

The appropriate mechanics have been derived to calculate the substrate's elastic moduli (E^s) from the composite's first order PS coefficients (Π_c) and a yield function has been used to obtain a consistent measure of Π_c for every PS response. Now, by applying Eq. (5), an elastic modulus map was created in Fig. 5A and a corresponding histogram in Fig. 5C. Due to a broad distribution within the histogram, uncertainty of the elastic modulus map was investigated before a comparison to *a priori* substrate elastic moduli values.

A significant number of points on the surface were identified to have large errors from experimental sources and a systematic uncertainty, described in the Appendix. When the local uncertainty of elastic modulus calculation exceeded 15.75 GPa, or 45% of the *a priori* known unnotched nominal modulus, the data points were filtered and these points on the elastic modulus map were replaced with white pixels in Fig. 5B post-filter. A significant amount of data points above and below the open hole contain white pixels because the longitudinal (ϵ_1) and transverse (ϵ_2) strains are nearly equal and opposite. This also combined with uncertainty from the algorithm used to align and interpolate the data sets based as discussed in the experiment section.

In addition, small regions directly above and below the hole contained negative values of Π_c , resulting in a negative E^s and they can be distinguished in Fig. 5A as white pixels pre-filter. These regions are the result of a compressive biaxial strain, but a tensile PS shift. Complex loading conditions associated with the non-proportional loading around the open hole are correlated to the observed negative moduli. One of the PS responses in this region that can be observed in Fig. 3C.

With the uncertainty issues addressed, the PS recorded moduli were compared to a previous test of control samples (16 unnotched) which determined that the nominal elastic modulus was 35 ± 3 GPa [25]. The modulus map in Fig. 5A shows a broad distribution of elastic modulus values with a mean centered at 32.2 GPa and a standard deviation of 9.4 GPa post-filter. The large number of data points taken across the surface produced a mean that closely resembles expected values for the unnotched, underlying substrate. The large standard deviation of the PS calculated moduli is proposed to be caused by an inhomogeneous dispersion of the nanoparticles, which is still an active field of research in the material's development [42]. These agglomerations lead to local variations in particle volume fraction, and thus particle–matrix load transfer mechanics [24].

As a damage measure, the elastic degradation of a material through mechanical loading [43] comes from the reduced effective stress carrying area by the presence of a crack or defect [44]. The latter results in an increase in stress on the remaining part of the material and is associated with a nominal reduction in stiffness [7]. For instance, the nominal modulus of the open hole tension composite coupon was 25 GPa, but the unnotched coupon was 35 GPa.

Conventionally, unloading curves during a mechanical test are used to monitor a reduced elastic modulus from the presence of damage [43]. This reduction in stiffness is referred to as elastic degradation. If unloading curves were not integrated in the experimental procedure, then the unloading curves may be simulated to estimate the reduced mechanical properties. Methods of simulating these unloading curves vary in complexity, ranging from simple elastic degradation models [7] to the involved continuum damage mechanics with coupled plasticity [7]. A simple and convenient method to simulate an unloading curve is to assume no plastic deformation so all unloading curves return to the origin, or contrarily, no elastic degradation and purely plastic deformation [7].

In reality, unloading is usually associated with a coupling between the elastic degradation and plastic deformation. Here, a

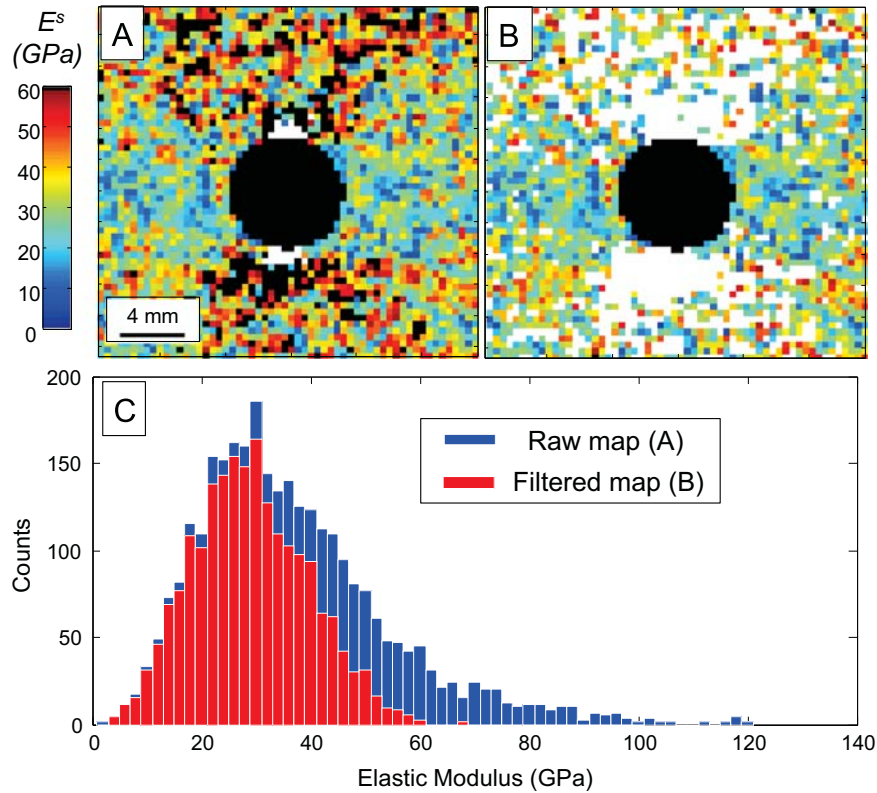


Fig. 5. Elastic modulus maps (A) before and (B) after the experimental uncertainty filter is applied. C, The corresponding histograms of the elastic modulus across the sample's surface.

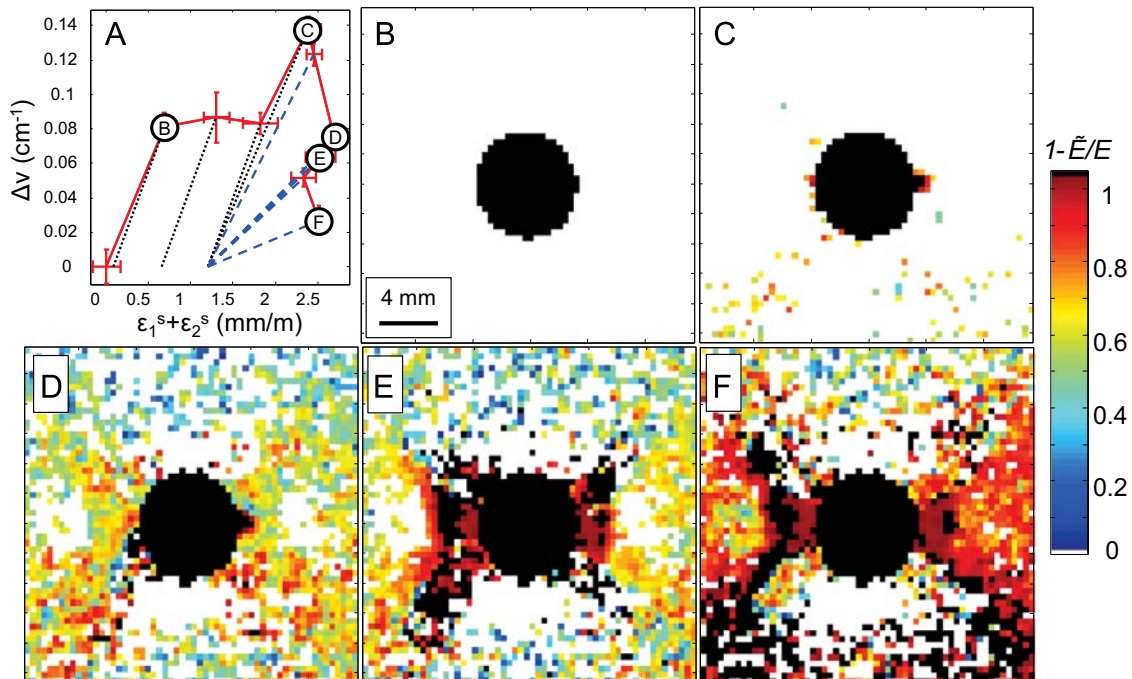


Fig. 6. (A) The simulation of the unloading curves for a PS response using plastic deformation until the max PS shift, after which purely elastic degradation is initiated. Loads which exhibited significant progression of damage are shown including (B) 0, (C) 76, (D) 88, (E) 92, and (F) 96 % failure load.

method for simulating unloading curves was used which included both plastic deformation and elastic degradation as shown in Fig. 6A. The simulated unloading curves only consider plastic deformation and no elastic degradation until the max PS shift has been reached. Further loading past the max PS shift ceases plastic deformation, and initiates elastic degradation.

The slopes of the simulated unloading curves on the PS response can be readily converted into an elastic modulus value with an isotropic damage assumption [36], that is Poisson's ratio remains constant. The degraded elastic modulus values (\tilde{E}) are normalized with respect to local pristine modulus (E), to create a damage measure ($D = 1 - \frac{\tilde{E}}{E}$) [8,43]. These damage maps reveal

intrinsic damage features of the composite substrate. Major turning points in the progression of damage are plotted in Fig. 6.

The first significant occurrence of damage is at 76% failure load just adjacent to the open hole. It is known *a priori* that this region should be experiencing large tensile strains, and is a likely location for damage to initiate. In other work by Camanho [45], a simulation using continuum damage mechanics of a transversely isotropic open hole tension composite coupon predicted initial fiber failure in the 0° ply in this exact region. Additionally, at 76% failure load, audible cracking in the sample suggest that significant damage had initiated.

The next significant progression of damage was at 88% failure load where homogeneous damage appeared across the sample's surface. This experimentally observed phenomena could be due to transverse cracking of the 90° plies which occurs homogeneously through the length of the sample [46]. In addition, literature has described a redistribution of stress occurring once subsurface damage has become significant [47]. This loading point is an important turning point in the mechanical test that may indicate the onset of critical damage.

Next, at 92% failure load, a large propagation of damage occurs on both sides of the open hole. A study using X-ray inspection has revealed similar cracking patterns [47] adjacent to the open hole in a tension test for a similar composite coupon. As the higher failure loads are reached, the damage pattern resembles intra-laminate cracking of the ±45° plies, and is very similar to predicted crack growth patterns with numerical models [47].

5. Conclusion

This work has successfully applied multi-scale mechanics to a PS coating experiment to obtain, for the first time, high spatial resolution damage maps using a degrading elastic modulus. Simulation of unloading curves *in situ* mechanical loading is used to estimate elastic degradation patterns which resemble intrinsic, subsurface damage patterns of the composite substrate [47,46,45]. In addition to locating the size and the location of damage, the ability to quantify the degradation of the elastic modulus enables the distinction of different types of damage. For example, matrix microcracking should change the equivalent modulus by a small amount in comparison to fiber failure or intra-laminate cracking. In the current study, the average uncertainty in the elastic modulus calculation was nearly 10 GPa and results in the detection of only critical damage. Future experiments will be designed to lower this uncertainty to detect more subtle changes in the effective elastic properties and adapt the coating to a wide range of substrates materials. An NDE technique that provides such a comprehensive damage characterization would be very desirable.

Acknowledgments

This material is based upon work supported by the National Science Foundation under Grant no. CMMI 1130837 and the University of Central Florida Office of Research and Commercialization Inhouse Grant FY 2012. Hong Tat, Gerardo Peña, and Jordan Handler from Boeing Research & Technology are acknowledged for technical discussions.

Appendix A. Elastic modulus uncertainty estimation

A filtering process was used to remove data points with high experimental error as shown in experimental uncertainties in the data collection varied from point to point based on a calculation of

a slope (Π_c), from local biaxial strain ($\epsilon_b = \epsilon_1 + \epsilon_2$) and PS shift data ($\Delta\nu$) in $\Delta\nu = \Pi_c \epsilon_b^s$. Here, $U_{\Delta\nu}$ and U_{ϵ_b} were taken as the error bars of the PS response at 20% failure load, which represents the standard deviation of local spatial variations calculated during the interpolation procedure of aligning the two data sets into a global coordinate system [27]. For the PS coefficient (U_{Π_c}), the systematic uncertainty varies across the surface of the sample with an average value of $38.1 \text{ cm}^{-1}\text{m/m}$ of all the post-filtered pixels using the following equation:

$$U_{\Pi_c}^2 = \left(\frac{\partial \Pi_c}{\partial \epsilon_b} U_{\epsilon_b} \right)^2 + \left(\frac{\partial \Pi_c}{\partial \Delta\nu} U_{\Delta\nu} \right)^2 \quad (\text{A.1})$$

$$U_{E^s}^2 = \left(\frac{\partial E^s}{\partial \Pi_c} U_{\Pi_c} \right)^2 + \left(\frac{\partial E^s}{\partial \Pi_{ii}} U_{\Pi_{ii}} \right)^2 + \left(\frac{\partial E^s}{\partial E^p} U_{E^p} \right)^2 + \left(\frac{\partial E^s}{\partial \nu^p} U_{\nu^p} \right)^2 + \left(\frac{\partial E^s}{\partial \nu^s} U_{\nu^s} \right)^2 \quad (\text{A.2})$$

This experimental uncertainty for Π_c is then plugged into the systematic uncertainty for the elastic modulus calculation given in Eq. (A.2). Every independent variable has its own uncertainty and contributes to the total uncertainty of the elastic modulus. The uncertainties for these values and their contribution to the total uncertainty are as follows: $U_{\Pi_{ii}} = 0.05 \text{ cm}^{-1}/\text{GPa}$, $U_{E^p} = 50 \text{ GPa}$, $U_{\nu^p} = 0.05$, $U_{\nu^s} = 0.05$, each contributing to the elastic moduli uncertainty calculation of 0.2, 3.3, 4.9, and 0.8 GPa respectively. Every pixel in the elastic modulus map has its own independent U_{Π_c} value, and the mean contribution to the elastic moduli uncertainty was 8.6 GPa. With all of the independent uncertainties combined, the mean experimental uncertainty for the substrate's elastic moduli calculation U_{E^s} was 10.5 GPa post-filtering. With this being the major contributing factor to the uncertainty, future work aims to design specialized equipment to capture the R-line peak shifts.

References

- [1] Kamsu-Foguem B. Knowledge-based support in non-destructive testing for health monitoring of aircraft structures. *Adv Eng Inf* 2012;26:859–69.
- [2] McCann D, Forde M. Review of NDT methods in the assessment of concrete masonry structures. *NDT & E Int* 2001;34:71–84.
- [3] Drinkwater BW, Wilcox PD. Ultrasonic arrays for non-destructive evaluation: a review. *NDT & E Int* 2006;39:525–41.
- [4] Bagavathiappan S, Lahiri B, Saravanan T, Philip J, Jayakumar T. Infrared thermography for condition monitoring—a review. *Infrared Phys Technol* 2013;60:35–55.
- [5] Francis D, Tatam RP, Groves RM. Shearography technology and applications: a review. *Meas Sci Technol* 2010;21:102001.
- [6] Zhu Y-K, Tian G-Y, Lu R-S, Zhang H. A review of optical NDT technologies. *Sensors* 2011;11:7773–98.
- [7] Carol I, Rizzi E, William K. A unified theory of elastic degradation and damage based on a loading surface. *Int J Solids Struct* 1994;31:2835–65.
- [8] Lemaitre J, Dufailly J. Damage measurements. *Eng Fract Mech* 1987;28(5/6):643–61.
- [9] Sharp B. Electronic speckle pattern interferometry (espi). *Opt Lasers Eng* 1989;11:241–55.
- [10] Walker CA. A historical review of Moiré interferometry. *Exp Mech* 1994;34:281–99.
- [11] Chu T, Ranson WF, Sutton M. Applications of digital-image-correlation techniques to experimental mechanics. *Exp Mech* 1985;25:232–44.
- [12] Horkay F, Lin DC. Mapping the local osmotic modulus of polymer gels. *Langmuir* 2009;25(15):8735–41.
- [13] Trtik P, Kaufmann J, Volz U. On the use of peak-force tapping atomic force microscopy for quantification of the local elastic modulus in hardened cement paste. *Cement Concr Res* 2012;42:215–21.
- [14] Giannoula A, Cobbold RS. Mapping the local shear modulus and viscosity using a transient finite-amplitude modulated radiation force. *Ultrasonics* 2011;51:340–51.
- [15] Sale M, Rizzo P, Marzani A. Semi-analytical formulation for the guided waves-based reconstruction of elastic moduli. *Mech Syst Signal* 2011;25:2241–56.
- [16] Frehofer G, Poliah L, Walker K, Medina A, Raghavan S. Optical stress probe: in situ stress mapping with R aman and photo-stimulated luminescence spectroscopy. *J Instrum* 2010;5:P12003.
- [17] Hanhan I, Durnberg E, Frehofer G, Akin P, Raghavan S. Portable piezospectroscopy system: non-contact in-situ stress sensing through high resolution photo-luminescent mapping. *J Instrum* 2014;9:P11005.

- [18] Piermarini GJ, Block S, Barnett JD, Forman RA. Calibration of the pressure dependence of the R_1 ruby fluorescence line to 195 kbar. *J Appl Phys* 1975;46:2774.
- [19] Christensen R, Lipkin D, Clarke D. Nondestructive evaluation of the oxidation stresses through thermal barrier coatings using Cr^{3+} piezospectroscopy. *Appl Phys Lett* 1996;69:3754–6.
- [20] Stevenson A, Jones A, Raghavan S. Stress-sensing nanomaterial calibrated with photostimulated luminescence emission. *Nano Lett* 2011;11:3274.
- [21] Freihofer G, Gupta A, Newkirk AV, Seal S, Raghavan S. Optical stress sensing alumina nanocomposite coatings for aerospace structures. In: AIAA SciTech, 55th AIAA/ASME/ASCE/AHS/SC structures, structural dynamics, and materials conference; 2014.
- [22] Freihofer G, Bullock A, Vaughn F, Tat H, Dustin J, Schülzgen A, et al. Stress and damage sensing of composite coupons with piezospectroscopic coatings. In: Proceeding of the society for the advancement of material and process engineering 2014 conference, Seattle, WA; 2014.
- [23] Freihofer G, Dustin J, Tat H, Schülzgen A, Raghavan S. Stress and structural damage sensing piezospectroscopic coatings validated with digital image correlation. *AIP Adv* 2015;5:037139.
- [24] Freihofer G, Schülzgen A, Raghavan S. Multi-scale mechanics to determine nanocomposite elastic properties with piezospectroscopy. *Acta Mater* 2014;81:211–8.
- [25] Marlett K. Hexcel 8552 im7 unidirectional prepreg 190 gsm & 35% rc qualification material property data report. Technical report. NIAR; 2011.
- [26] ASTM. D5766/D5766M-11 standard test method for open-hole tensile strength of polymer matrix composite laminates. West Conshohocken, PA: ASTM International; 2011.
- [27] Freihofer G. Nanocomposite coating mechanics via piezospectroscopy [Ph.D. thesis]. University of Central Florida; 2014.
- [28] He J, Clarke DR. Determination of the piezospectroscopic coefficients for chromium doped sapphire. *J Am Ceram Soc* 1995;78(5):1347–53.
- [29] Lipkin D, Clarke D. Measurement of the stress in oxide scales formed by oxidation of alumina-forming alloys. *Oxid Metals* 1996;45:267.
- [30] Ma Q, Clarke DR. Piezospectroscopic determination of residual stresses in polycrystalline alumina. *J Am Ceram Soc* 1994;77:298–302.
- [31] He J, Beyerlein IJ, Clarke DR. Load transfer from broken fibers in continuous fiber Al_2O_3 -Al composites and dependence on local volume fraction. *J Mech Phys Solids* 1999;47:465–502.
- [32] Marur P, Batra R, Garcia G, Loos A. Static and dynamic fracture toughness of epoxy/alumina composite with submicron inclusions. *J Mater Sci* 2004;39(4):1437–40.
- [33] Cho J, Joshi M, Sun C. Effect of inclusion size on mechanical properties of polymeric composites with micro and nano particles. *Compos Sci Technol* 2006;66:1941–52.
- [34] Deng F, Vliet K. Prediction of elastic properties for polymer-particle nanocomposites exhibiting an interphase. *Nanotechnology* 2011;22:165703.
- [35] Munro RG. Evaluated material properties for a sintered α alumina. *J Am Ceram Soc* 1997;80:1919–28.
- [36] Hansen N, Schreyer H. A thermodynamically consistent framework for theories of elastoplasticity coupled with damage. *Int J Solids Struct* 1994;31:359–89.
- [37] Reddy J, Miravete A. Practical analysis of composite laminates. Boca Raton, FL: CRC Press, Inc.; 1995.
- [38] Withers P. The determination of the elastic field of an ellipsoidal inclusion in a transversely isotropic medium, and its relevance to composite materials. *Philos Mag A* 1989;59:759–81.
- [39] Zhu Y, Liu E. Approximate Eshelby tensor for transversely isotropic media. In: Society of exploration geophysicists; 2011.
- [40] Kontou E. Micromechanics model for particulate composites. *Mech Mater* 2007;39(7):702–9.
- [41] Lubliner J. Plasticity theory. Mineola, NY: Dover Publications; 2008.
- [42] Stevenson A, Jones A, Raghavan S. Characterization of particle dispersion and volume fraction in alumina-filled nanocomposites using photo-stimulated luminescence spectroscopy. *Polymer* 2011;43:923–9.
- [43] Alves M, Yu J, Jones N. On the elastic modulus degradation in continuum damage mechanics. *Comput Struct* 2000;76(6):703–12.
- [44] Luo AC, Mou Y, Han RP. A large anisotropic damage theory based on an incremental complementary energy equivalence model. *Int J Fract* 1995;70:19–34.
- [45] Camanho PP, Maimí P, Dávila C. Prediction of size effects in notched laminates using continuum damage mechanics. *Compos Sci Technol* 2007;67(13):2715–27.
- [46] Vinogradov V, Hashin Z. Probabilistic energy based model for prediction of transverse cracking in cross-ply laminates, *Int J Solids Struct* 2005;42:365–92.
- [47] Mollenhauer D, Larve E, Kim R, Langley B. Examination of ply cracking in composite laminates with open holes: a moiré interferometric and numerical study. *Compos Part A: Appl Sci Manuf* 2006;37:282–94.